Influence of CME Interaction on Propagation of Interplanetary Shocks

P.K. Manoharan[1,2], N. Gopalswamy[3], S. Yashiro[1], A. Lara[1,4], G. Michalek[1,5], and R.A. Howard[6]

Abstract.

We studied 91 interplanetary (IP) shocks associated with coronal mass ejections (CMEs) originating within about ±30° in longitude and latitude from the center of the Sun during 1997 – 2002. These CMEs cover a wide range of initial speeds of about 120 to 2400 kms^{-1} and they also include a special population of 25 interacting CMEs. This study provides the characteristics of propagation effects of more number of high-speed CMEs (V_{CME}>1500 kms^{-1}) than the data used in earlier studies. It enables to extend the shock-arrival prediction model to high-speed CMEs. The results on comparison of IP shock speed and transit time at 1 AU suggest that the shock transit time is not controlled by its final speed, but is primarily determined by the initial speed of the CME and effects encountered by it during the propagation. It is found that the CME interaction tends to slow the shock and associated CME. The deviations of shock arrival times from the empirical model are considerably large for slow (V_{CME}<300 kms^{-1}) and fast (V_{CME}>800 kms^{-1}) CMEs. Results show that the slow and fast CMEs experience stronger effective acceleration.

1. Introduction

Observations of intense shock wave disturbances near 1 AU show a direct association with coronal mass ejections (CMEs) from the Sun. Recent space missions (e.g., Solar Heliospheric Observatory (SOHO), Wind, and Advance Composition Explorer (ACE)) have shown the ability to image the earth-directed CMEs leaving the Sun and to observe 1–5 days later their plasma and magnetic field properties in the near-earth space. Given the observations of a CME eruption, an understanding of the effects of CME on geospace is essential for the solar-terrestrial studies as well as forecasting the space weather.

There is considerable interest to predict magnetic field orientations, speeds and arrival times of CMEs at the near-earth space. Several authors have attempted to link the near-Sun observations of CMEs with those of their interplanetary counterparts: (1) to assess their geomagnetic effects and (2) to estimate the travel time to 1 AU. [e.g., *Gopalswamy et al.,* 2000, 2001a, 2004; *Webb et al.,* 2000; *Srivastava and Venkatakrishnan,* 2002; *Cane and Richardson,* 2003; *Vilmer et al.,* 2003; *Zhang et al.,* 2003]. Concerning the propagation of CMEs, Gopalswamy and his co-workers [*Gopalswamy et al.,* 2001a] proposed an empirical relation to predict the arrival times of CMEs based on their speed measurements near the Sun and at 1 AU. This kinematical model has also been extended to predict the arrival of associated IP shocks [*Gopalswamy et al.,* 2004]. However, since the solar wind consists of both ambient quasi-steady state components as well as shocks, discontinuities and multi-speed streams, all of them can interact with a propagating CME and likely to play a significant role on the arrival time at 1 AU of the CME and shock.

Recently, *Gopalswamy et al.* [2002a,b; 2003] have shown that CME interaction is an important aspect for the SEP production. CMEs causing large SEP events interact and overtake slower CMEs on their way. These studies suggest that the CME interaction enhances the efficiency of the CME-driven shock, which can accelerate SEPs from the magnetized plasma of the preceding slow CME. Therefore, it is essential to understand the propagation characteristics of IP shocks associated with the interacting CMEs. We consider here the propagation of IP shocks associated with 25 interacting CMEs.

2. Data Selection

In this study, our objective is to characterize the propagation properties of CMEs and their related shocks observed during 1997 – 2002. We identify all IP shocks and analyze their plasma and magnetic field properties at 1 AU. The CMEs associated with these shocks are identified using white-light measurements obtained from Large Angle and Spectrometric Coronagraph (LASCO) and full disk images from Extreme ultraviolet Imaging Telescope (EIT) on board Solar Heliospheric Observatory (SOHO) mission. However, in this study, we select only those IP shocks associated with disk-center (within about ±30° from the center of the Sun) CMEs. We also consider shocks associated with the interacting CMEs as a special population. We compare the travel times of IP shocks to 1 AU with the shock-arrival model given by *Gopalswamy et al.* [2004]. The estimated errors obtained between models and observed travel times are discussed.

We consider shock wave disturbances detected by the Wind spacecraft during 1997 – 2002 (http://www-spof.gsfc.nasa.gov/wind/), supplemented with the shock lists obtained from Proton Monitor (PM) instrument on

[1]Center for Solar Physics and Space Weather, The Catholic University of America Washington, DC., USA.

[2]Tata Institute of Fundamental Research, Radio Astronomy Centre, Ooty (Udhagamandalam), India.

[3]NASA Goddard Space Flight Center, Greenbelt, Maryland, USA.

[4]Instituto de Geofisica, Universidad Nacional Autonoma de Mexico, Mexico City, Mexico.

[5]Astronomical Observatory of Jagiellonian University, Cracow, Poland.

[6]Naval Research Laboratory, Washington, D.C., USA.

0148-0227/04/$9.00

board SOHO mission (http://umtof.umd.edu/pm/) and ACE spacecraft (http://www.bartol.udel.edu/ace/). By examining solar wind plasma data (from Solar Wind Experiment (Wind/SWE) instrument, http://web.mit.edu/space/www/wind/) and interplanetary magnetic field data (from Magnetic Field Investigation (Wind/MFI) instrument, http://lepmfi.gsfc.nasa.gov/mfi/), we identified 163 IP shocks and their associated interplanetary CMEs (ICMEs). For each event, we determine the shock onset time, shock speed, Mach numbers (Alfvenic Mach number, M_a and magnetosonic Mach number, M_s), and approximate start time and average speed of the associated ICME (ejecta or magnetic cloud). We are interested in comparing the IP shock properties with those of white-light CMEs. Hence, we have excluded periods of data gaps in LASCO as well as solar wind measurements. Further, we consider an IP shock only when its associated ICME measurements are available. Therefore, the IP shocks reported in this study represent a subset of CME-driven shocks.

For an IP shock at the earth, its potential CME near the Sun has been identified within a time frame of 1 to 5 days backward from the onset time of the shock. While tracing the CME origin to the Sun, we have taken into account the observed speed of the shock at 1 AU and initial speed (also width and location) of the CME. The LASCO and EIT images, movies, and speed data obtained from the SOHO mission have been systematically cataloged [http://cdaw.gsfc.nasa.gov/; *Yashiro et al.*. 2004]. In order to identify the location of the solar activity likely associated with a CME, the above LASCO and EIT movies have been used along with the flare list provided by NOAA (ftp://ftp.sec.noaa.gov/). Whenever required, the available Yohkoh – SXT images have also been employed to locate the CME on the Sun. However, when multiple CMEs were observed at the Sun, it was difficult to make a unique identification of the white-light CME. For example, during November 23–30, 2000, a series of fast and wide CMEs occurred from different regions on the Sun. They caused complex activities at the near-earth space. For the above period, we include 2 CMEs (on 00/11/24 at 05:30 and 1530 UT) and their IP shocks. However, during such period, associating a CME to an IP shock is likely to have uncertainty.

The location of a CME on the Sun and its width are crucial in determining the effect of the 'shock – CME' pair at 1 AU. For example, the near-earth observation of an IP shock associated with a CME originating close to the solar limb cannot reveal the nature of the shock nose and its related portion of the driver CME (i.e., the piston). It can only show the characteristics at the edge of the shock [*e.g., Borrini et al.,* 1982]. Moreover, it has been reported that most of the geoeffective CMEs originate close to the center of the Sun [*e.g., Gopalswamy,* 2002]. Therefore, in this study, we select 91 IP shocks, which are associated with CMEs originating close to the center of the Sun, within about 30° from the Sun's center. *Gopalswamy et al.* [2001a, 2003] investigated 47 CMEs between December 1996 and July 2000 and 29 CMEs between January 1997 and May 2002. The present list includes 36 disk-center events from these above studies.

We identify the ICME associated with an IP shock, by examining the solar wind plasma data (proton density, speed, and temperature) as well as magnetic field measurements followed after the IP shock onset. There are a number of plasma and magnetic field features associated with ICMEs (i.e., interplanetary ejecta (EJ) of CMEs) [*e.g., Neugebauer and Goldstein,* 1997; *Lepping et al.,* 1997]. However, we identify ejecta using (1) low proton temperature, (2) strong magnetic field, and (3) a smooth rotation in the magnetic field direction indicative of a magnetic cloud (MC). MCs are a subset of ejecta. For a few events, high charge state of iron has also been examined to identify the ICME plasma. The presence of these signatures singly or together varied from one ICME to the other.

In general, most of the shocks associated with earth-directed CMEs are observed with accompanying ICMEs. However, events traveling perpendicular or at an angle (>45°) to the Sun-Earth line are likely to cause shock-wave like disturbances at 1 AU, but their ICMEs may not pass through the earth. The selection criteria imposed on the source location of white-light CMEs (±30° from the center of the Sun) would exclude all such cases. However, for example, 2 IP shocks associated with disk center events showed no clear accompanying ICMEs at 1 AU. The shock on 97/10/24, 11:15UT (associated halo CME on 97/10/21, 18:04UT at N16E07) showed large fluctuations in solar wind density (about 15 to 60 ions/cm^3) after the shock passage. It is likely that the shock passed through high-density structures in the solar wind. In a second case (01/03/27 02:02UT, associated halo CME on 01/03/24 20:50UT at N15E22), the IP shock was followed by another shock (also its ICME) about 16 hours later. The white-light CMEs of these IP shocks originated from the same region on the Sun with a time separation of ~20 hours. It is likely that the later CME interacted with the preceding one and the observed ICME signatures are effects of both CMEs. Such events having ambiguous identification of ICMEs have not been included in the present study.

Gopalswamy et al. [2002b, 2003] studied the interaction of CMEs associated with large solar energetic particle (SEP) events. We use their lists to select interacting cases that overlapped with some of our disk center events. We have also examined EIT and LASCO (C2 and C3) images obtained from the SOHO mission to identify the interaction of the primary CME with any preceding CME(s) within the LASCO field of view, i.e., $\leq$30 $R_\odot$. These interactions, however, have only been considered for (i) CMEs originating from the same region (or close to the location of the preceding CME) on the Sun and (ii) CMEs leaving the Sun within a day before the primary CME. The above conditions have been imposed to ascertain the interaction. Figure 1 shows the locations of CMEs associated with the 163 IP shocks observed at 1 AU during 1997 – 2002. Circles (91 data points) correspond to CMEs originating within ±30° of the Sun. The interacting CMEs (25 events) are shown by filled circles. Table 1 gives date, time, and parameters of the 91 IP shocks and the associated CMEs.

3. IP Shock Speed and Transit Time at 1 AU

The propagation time of the IP shock is estimated as, $t_{shock} = t_2 - t_1$, where t_2 is the shock arrival time at the Wind spacecraft. The time of first appearance of the CME in the LASCO-C2 field of view (at a height $\geq$2 $R_\odot$) is assumed to be the start time of the CME as well as the shock, t_1. This assumption is good for the shocks associated with the fast CMEs. However, due to the limitation of shock information in the near-Sun region, it is also reasonable to assume such start time for the shocks associated with the low-speed CMEs. As shown in Table 1, most of the IP shocks are fairly strong and the Alfvenic Mach numbers (computed from the upstream and downstream density, magnetic field and temperature) fall in the range 1.1 to 9.0, with an average value of 2.9. The IP shock speed and the average ICME speed measured at 1 AU are linearly correlated (correlation coefficient ≈ 85%). The average ratio between these speeds is 1.2. Above results confirm the 'piston–shock' relation, $V_{SHOCK} = V_{ICME}(1+\gamma)/2$, where γ is the ratio of specific heats [see, *e.g., Landau and Lifshitz,* 1987]. The CME-arrival prediction model is extended to predict the transit time of shock following *Gopalswamy et al.* [2004].

Most of the associated CMEs are fairly wide (77 CMEs have plane of sky widths greater than 160°) and the majority of them are halo CMEs. For a halo CME, LASCO images provide a speed projected on to the plane of the sky. However, a separate study of wide limb CMEs indicates that their radial propagation speeds are about 90% of the lateral expansion speeds [*Manoharan, Gopalswamy, and Yashiro, in preparation*]. Similar result has been obtained for 54 limb CMEs [*Dal Lago, Schwenn, and Gonzalez*, 2003]. Such large CMEs would appear as halos if they were viewed along the propagation direction (also, as in the present study, they would be halos if they were earth-directed CMEs). In this study, a linear fit to the 'height-time' plot of the CME leading edge (measured close to the center of the CME) has been considered as its radial speed and no correction has been made for the projection effect. The initial speeds of the CME range between 123 to 2411 kms^{-1}, with an average of $<V_{CME}>\sim$732 kms^{-1}. Table 2 shows the averages and ranges of observed parameters, separately, for all 91 events and 25 interacting cases.

Figure 2 shows the observed shock transit time as a function of IP shock speed at 1 AU. A large scatter is observed in travel time for a given shock speed. In the plot, filled circles represent CMEs possibly interacting with preceding CME(s). For a given shock transit time, interacting cases have a smaller shock speed at 1 AU. However, as shown in Table 2, the average CME initial speed of interacting cases is $<V_{CME}>$ = 973 kms^{-1}. In other words, mostly, fast CMEs interact with the preceding CME(s). It is likely that the interaction between CMEs (1) tends to reduce the speed of the shock at the point of interaction, and/or (2) modifies the characteristics of the shock to decelerate it faster than the non-interacting cases. These results suggest that the final shock speed is not indicative of the shock transit time, which is largely determined by the propagation effects and initial speed of the CME. However, the tendency of decreasing of travel time with shock speed is due to the correlation between CME and IP shock speeds (see, Figure 3).

In Figure 2, the data points overplotted with a 'triangle' symbol indicate IP shocks associated with CMEs having low initial speed, (i.e., $V_{CME} \leq$ 375 kms^{-1}). However, the final speeds of almost all shocks lie in the range of 350 to 850 kms^{-1}. One possibility is that we consider only earth-directed events, for which speed estimates from white-light measurements, as mentioned above, are likely affected by projection effects. Next, IP shocks associated with slow CMEs ($V_{CME} \leq$ 375 kms^{-1}) may experience gradual acceleration. On the other hand, shocks associated with CMEs of speed higher than the ambient solar wind flow ($V_{ambient}\approx$400 kms^{-1}) experience a medium to large deceleration. In Figure 2, a second-order least-square fit to the data points, shown by a solid line, provides the transit time as a function of shock speed (kms^{-1}) at 1 AU as given by, t_{shock} (days) = 5.4 - 6.7×10^{-3} V_{shock} + 3.4×10^{-6} V^2_{shock}.

4. Initial and Final Speeds of CMEs and IP Shocks

Figure 3 shows the observed IP shock speed at 1 AU plotted against the associated CME's initial speed (V_{CME} is obtained from a linear fit to the LASCO 'height-time' measurements). As before, all filled circles indicate the interacting CMEs. It is evident from the figure that for a given V_{CME}, shocks at 1 AU show a large scatter in speed. However, the CME and shock speeds show a correlation coefficient of ~60%. The speeds corresponding to the interacting CMEs form the lower envelope of the distribution.

Various curves shown in Figure 3 are from the model given by *Gopalswamy et al.* [2001a]. This empirical model is based on initial speed near the Sun and final speed near the earth. The dependence of resultant acceleration, a (ms^{-2}), on the initial speed of the CME, V_{CME} (kms^{-1}), is given by,

$$a = 2.2 - 5.4 \times 10^{-3}\ V_{CME} \quad (1)$$

and

$$a = 1 - 5.5 \times 10^{-4}\ V_{CME} - 3.2 \times 10^{-6}\ V^2_{CME}, \quad (2)$$

respectively, for the linear and quadratic fits to the speed data. While predicting the arrival of CMEs at 1 AU, *Gopalswamy et al.* [2001a] also considered the cessation of acceleration of the CME at some distance, d_1, from the Sun. That is, the acceleration continues as shown by the above equations up to about a distance d_1 and for the remaining distance, d_2, (d_2 = 1 AU - d_1), the CME is assumed to travel with a constant speed. Therefore, the CME speed at 1 AU can be obtained from the relation, $V^2 = V^2_{CME} + 2\ a\ d_1$. We used the final speed of CMEs to obtain the final speed of IP shocks using piston-shock relationship as described in *Gopalswamy et al.* [2004].

In the above 'V_{SHOCK} - V_{CME}' plot (Figure 3), we notice two branches. (1) The first one showing a steep increase in shock speed. Although dominated by a single point corresponding to the well observed Bastille Day event [*e.g., Manoharan et al.,* 2001; *Tokumaru et al.,* 2003], it is in agreement with the linear acceleration model (equation 1) of *Gopalswamy et al.* (2) The second branch shows a relatively slow increase in shock speed as a function CME speed and the observed travel times are consistent with the quadratic fit (equation 2) for an acceleration cessation distance, $d_1 \sim$ 0.95 AU. In Figure 3, the curves for the different cessation distances are indicated by different line thicknesses.

The best-fit curve (solid curve) to the data points shown in Figure 3 is given by,

$$V_{SHOCK} = 420 + 0.2\ V_{CME} + 2.3 \times 10^{-5}\ V^2_{CME}. \quad (3)$$

Most of the interacting cases shown by the filled circles fall below or on the best-fit curve. It may be noted that a best-fit obtained separately for the interacting cases falls below the curve obtained from the remaining open-circle points. We also examine four other data points falling below or on the best-fit line (equation 3): (1) 01/10/22 (see Table 1, Sr. no. 72, V_{CME} = 1336 kms^{-1}), (2) 01/11/04 (Sr. no. 75, V_{CME} = 1810 kms^{-1}), (3) 02/08/16 (Sr. no. 88, V_{CME} = 1459 kms^{-1}), and (4) 02/09/05 (Sr. no. 90, V_{CME} = 1657 kms^{-1}). These points are indicated by letters a, b, c, and d on the figure. The first two events have been studied by *Gopalswamy et al.* [2002b] in the SEP aspect and they are interacting cases. Since we consider interaction of CMEs from the same region, the first one is not included as an interacting case in our list. The second one however interacts with bright streamers in the western side as seen in LASCO images. The third and fourth events also show interactions with CMEs, but originating from different locations on the Sun. It is likely that some of the other lower envelope data points, falling below the best-fit line, may also be due to the influence of interaction with streamers, wide CMEs from nearby location of the Sun or interaction at larger distances (outside LASCO field of view).

The above results reveal that the CME-arrival model [*Gopalswamy et al.,* 2001a] with an acceleration-cessation distance, d_1, in the range 0.75 to 1 AU can explain the propagation of majority of the ICME – IP shock pairs. Further, the best-fit acceleration cessation distance, d_1, whether toward the lower end ($\leq$0.75 AU) or at the earth distance, indicates the severity of interaction experienced by the CME with other preceding CME(s) and/or with solar wind to be strong or weak.

5. CME Initial Speed and Shock Transit Time

In Figure 4, the observed travel time of IP shock is plotted as a function of its CME initial speed. The shocks associated with CME speeds, V_{CME}<500 kms^{-1}, are consistent with model curves obtained from linear fit [equation 1; *Gopalswamy et al.,* 2001a]. In the case of fast CMEs, the second order acceleration fit curves (equation 2) lie closer to the observed data points than the constant acceleration curves. It is to be noted that the present study includes more number of faster CMEs (V_{CME}>1500 kms^{-1}) than the data used for obtaining equations 1 and 2.

As seen in Figure 4, for a given initial speed of the CME, a wide range of transit times are observed (minimum to maximum varies between 1.5 to 2 days). In particular, a large scatter is observed when the initial speed of the CME is low, $V_{CME} \leq 450$ kms^{-1}. The solid line is the best fit curve to all the data points and it gives a shock transit time,

$$t_{shock} = 3.9 - 2 \times 10^{-3}\ V_{CME} + 3.6 \times 10^{-7}\ V_{CME}^2 \quad (4)$$

where the initial speed of the CME is given in kms^{-1} and t_{shock} is given in days. The best-fit curve also can be used to obtain the change in acceleration with the initial speed of the CME, as given by,

$$a = 2.3 - 1.8 \times 10^{-3} V_{CME} - 2.9 \times 10^{-6} V_{CME}^2. \quad (5)$$

This acceleration profile (equation 5) is similar to the one given in equation 2, except it shows a rapid fall for higher-speed CMEs. Note that equations 1 and 2 were obtained from CMEs of speeds $\leq$1600 kms^{-1}. The above empirical relation for the transit time of an IP shock (equation 4) provides a suitable model for shocks associated with low and high-speed CMEs. However, some of the shocks show large deviation ($\sim$20 hours) from the best-fit curve (see Figure 4). The examination of these cases shows that most of them are associated with interacting CMEs and/or low-speed CMEs (see discussion below).

Figure 5 shows the histograms of distribution of estimated errors between the models and observations. The zero-centered histogram (top panel) is for errors between the best-fit (equation 4) and observations. The middle panel is the error distribution obtained between equation 1 and observations for an acceleration cessation distance, $d_1 = 0.95$ AU. It has an offset of about +5 hours. The bottom panel corresponds to equation 2 and it is centered at –5 hours. However, the mean absolute deviations (i.e., mean of magnitude of deviations) for these distributions are quite similar and they are 10, 14, and 11 hours, from top to bottom. The mean deviation obtained for the best-fit model (equation 4) indicates the accuracy of the predicted arrival times and supports the basis of the models used in the prediction.

In Figure 4, for a given CME speed, the interacting cases also show similar scatter in the arrival times. We examined 13 cases having 20 hours or more of travel time deviation from the empirical model given in equation 4. This reference model has been obtained from the best fit to all the data points. Out of these, 8 events showed longer travel times than the prediction curve and the rest of them were shorter than the prediction. In the longer-travel time group, 5 cases were associated with clear and probable interaction candidates of fast CMEs (see Section 4 and Figure 3) and remaining 3 events were associated with slow CMEs (V_{CME} < 270 kms^{-1}). It is likely that the propagation of CME events having shorter travel times than the best-fit curve is supported by the solar wind flow. As shown in Figure 6, the absolute deviations in travel times between the prediction and observation show two peaks, (1) for V_{CME}<400 kms^{-1} and (2) for V_{CME}>750 kms^{-1}. These results suggest that the effective acceleration is stronger for both slow and fast CMEs. The acceleration is essentially determined by the interaction of CMEs with solar wind and preceding CME(s).

In continuation of the above discussion, in Figure 4, data points showing smaller deviation from the empirical model (i.e., equation 4) and lying on the best-fit line indicate that these CMEs experience lesser influence of interaction in the solar wind. They provide an average characteristics of propagation of IP shocks in the less-disturbed solar wind condition.

6. Discussion and Conclusions

In this study, we have examined 91 IP shocks associated with CMEs originating from within about ±30° in longitude and latitude from the disk center during 1997 – 2002. These CMEs have a wide range of initial speeds, 120 – 2400 kms^{-1}and also include 25 interacting CMEs with preceding CME(s) within the LASCO field of view and within about a day. Figures 3 and 4 show that for large CME speeds, the travel time of the shock is primarily determined by the initial speed of the CME. However, the number of data points is small in the high-speed range. The prediction of shock arrival times as an extension of the CME arrival model [*Gopalswamy et al.,* 2001a; 2004] is consistent with these observations.

As shown in Figure 2, the majority of the shocks observed at 1 AU narrow down to speed within about ±150 kms^{-1}of the ambient solar wind ($V_{ambient}$ ≈400kms^{-1}). The IP shock speed at 1 AU of interacting CMEs falls below the best-fit curve (Figures 2 and 3), indicating that the interacting ones decelerate more than the non-interacting CMEs. However, for a given CME speed, a large scatter seen in the transit times of the shock indicates that each CME goes through different propagation effects. The deviation of arrival time from the empirical model (equation 4) shows that the effective acceleration imposed on slow and fast CMEs are stronger. It is consistent with the idea of drag force [e.g., *Gopalswamy et al.,* 2001b], which is proportional to the square of the difference in speeds between interacting CME and the solar wind as well as between interacting CMEs. As discussed in Section 2, the absence of ICME after the IP shock associated with a disk center event is likely to be caused by the interaction. Since a shock can propagate without much of hindrance, however, when the CME merges with the solar wind due to interaction, the ICME signatures may be absent at 1 AU.

In summary, this study has enabled us to extend the empirical arrival time prediction model to high initial speed of the CME ($\sim$2500 kms^{-1}). As shown by equation 4, the shock transit time depends on the initial speed of the CME. This study also suggests that the CME interaction tends to slow the shock and associated ICME.

Acknowledgments. We thank Drs. R.P. Lepping and D. Berdichevsky for Wind/MFI data, K. Ogilvie for Wind/SWE data, and F. Ipavich for SOHO/MTOF data on IP shocks. This research was supported by NASA/LWS, AFOSR, and NSF/SHINE (ATM 0204588) programs. The work done by G. Michalek was partly supported by *Komitet Badań Naukowych* through the grant PBZ-KBN-054/P03/2001.

References

Borrini, G., J.T. Gosling, S.J. Bame, and W.C. Feldman, An analysis of shock wave disturbances observed at 1 AU from 1971 through 1978, *J. Geophys. Res., 87*, 4365, 1982.

Cane, H.V. and I.G. Richardson, Interplanetary coronal mass ejections in the near-Earth solar wind during 1996-2002, *J. Geophys. Res., 108*, 1156, 2003.

Dal Lago, A., R. Schwenn, and W.D. Gonzalez, Relationship between the radial speed and the expansion speed of coronal mass ejections, *Adv. Space Res., 32*, 2637, 2003.

Gopalswamy, N., Relationship between coronal mass ejection and their interplanetary counterpart, in Solar-Terrestrial magnetic activity and space environment, *COSPAR Colloquia Series, eds. H.N. Wang and R.L. Xu, 14*, 157, 2002.

Gopalswamy, N., A. Lara, R.P. Lepping, M.L. Kaiser, D. Berdichevsky, and O.C. St Cyr, Interplanetary acceleration of coronal mass ejections, *Geophys. Res. Lett., 27*, 145, 2000.

Gopalswamy, N., A. Lara, S. Yashiro, M.L. Kaiser, and R.A. Howard, Predicting the 1-AU arrival times of coronal mass ejections, *J. Geophys. Res., 106*, 29207, 2001a.

Gopalswamy, N., S. Yashiro, M.L. Kaiser, R.A. Howard, and J.-L. Bougeret, Characteristics of coronal mass ejections associated with long wavelength type II radio bursts, *J. Geophys. Res.,* , 106, 29219, 2001b.

Gopalswamy, S. Yashiro, M.L. Kaiser, R.A. Howard, J.-L. Bougeret, Interplanetary radio emission due to interaction between two coronal mass ejections, *Geophys. Res. Lett., 29*, 1265, 2002a.

Gopalswamy, N., S. Yashiro, G. Michalek, M.L. Kaiser, R.A. Howard, D.V. Reames, R. Leske, and T. von Rosenvinge, Interacting coronal mass ejections and solar energetic particles, *Astrophys. J., 572*, L103, 2002b.

Gopalswamy, N., S. Yashiro, G. Stenborg, and R. Howard, Coronal and interplanetary environment of large solar energetic particle events, *Proc. 28th International Cosmic Ray Conference, Universal Academy Press*, p3549, 2003.

Gopalswamy, N., A. Lara, P.K. Manoharan, and R.A. Howard, An empirical model to predict the 1-AU arrival of interplanetary shocks, *Adv. Space Res.*, 2004, in press.

Landau, L.D. and E.M. Lifshitz, *Course of Theoretical Physics, Fluid Dynamics, vol. 6, Pergamon Press, New York*, p.347, 1987.

Lepping, R.P., L.F. Burlaga, A. Szabo, K.W. Ogilvie, W.H. Mish, D. Vassiliadis, A.J. Lazarus, J.T. Steinberg, C.J. Farrugia, L. Janoo, and F. Mariani, The Wind magnetic cloud and events of October 18-20, 1995: Interplanetary properties and as triggers for geomagnetic activity, *J. Geophys. Res., 102*, 14049, 1997.

Manoharan, P.K., M. Tokumaru, M. Pick, P. Subramanian, F. M. Ipavich, K. Schenk, M. L. Kaiser, R. P. Lepping, and A. Vourlidas, Coronal mass ejection of 2000 July 14 flare event : Imaging from near-Sun to Earth environment, *Astrophys. J., 559*, 1180, 2001.

Neugebauer, M., and R. Goldstein, Particle and field signatures of coronal mass ejections in the solar wind, in N. Crooker et al. (eds.), Coronal Mass Ejection, *AGU Monograph 99*, 245, 1997.

Srivastava, N. and P. Venkatakrishnan, Relationship between CME speed and geomagnetic storm intensity, *Geophys. Res. Lett., 29*, 1287, 2002.

Tokumaru, M., M. Kojima, K. Fujiki, M. Yamashita, and A. Yokobe, Toroidal-shaped interplanetary disturbance associated with the halo coronal mass ejection event on 14 July 2000, *J. Geophys. Res., 108*, 1220, 2003.

Vilmer, N., M. Pick, R. Schwenn, P. Ballatore, and J.P. Villain, On the solar origin of interplanetary disturbances observed in the vicinity of the Earth, *Annales Geophysicae, 21*, 847, 2003.

Webb, D.F., E.W. Cliver, N.U. Crooker, O.C. St Cyr, and B.J. Thompson, Relationship of halo coronal mass ejections, magnetic clouds, and magnetic storms, *J. Geophys. Res., 105*, 7491, 2000.

Yashiro, S., N. Gopalswamy, G. Michalek, O.C. St Cyr, S.P. Plunkett, N.B. Rich, and R.A. Howard, A catalog of white-light coronal mass ejections observed by the SOHO spacecraft, *J. Geophys. Res., submitted.*

Zhang, J., K.P. Dere, R.A. Howard, and V. Bothmer, Identification of solar sources of major geomagnetic storms between 1996 and 2000, *Astrophys. J., 582*, 520, 2003.

N. Gopalswamy, A. Lara, P.K. Manoharan, G. Michalek, S. Yashiro, NASA Goddard Space Flight Center, Code 695.0, Greenbelt, MD 20771, USA. (mano@cspsw3.gsfc.nasa.gov)

R.A. Howard, Space Science Division, Naval Research Laboratory, Washington, DC 20375, USA.

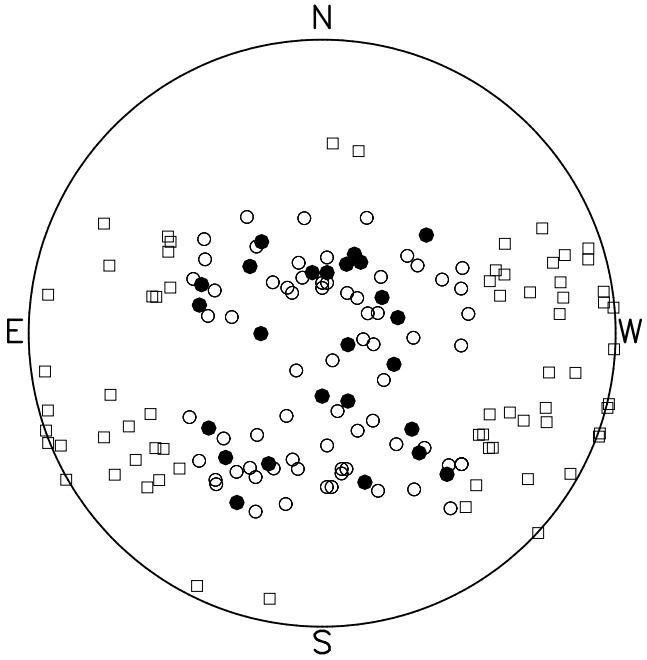

Figure 1. Distribution of source location of CMEs associated with the 163 IP shocks observed at 1 AU during 1997–2002. Circles (91 data points) correspond to ±30° in longitude and latitude from the center of the Sun. The filled circles represent CMEs possibly interacting with one or more preceding CMEs. The plotted location is for surface activity likely associated with each CME.

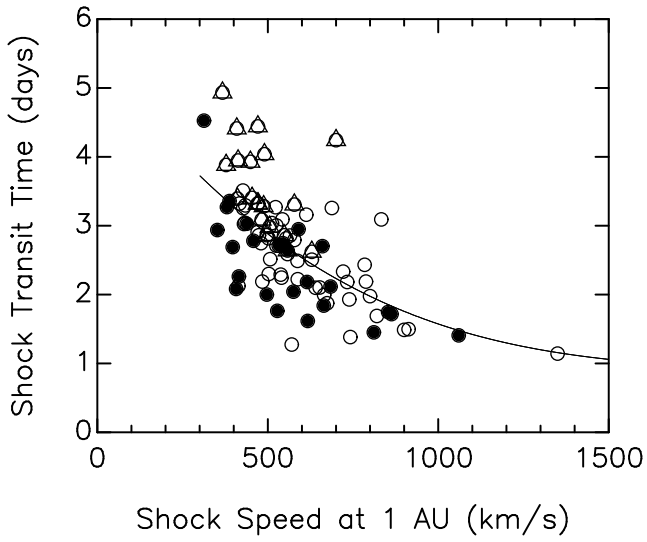

Figure 2. Observed IP shock speed at 1 AU as a function of its travel time from Sun to Earth. The second-order least square fit to the data points is shown by the solid line (t_{shock} = 5.4 - 6.7×10^{-3} V_{shock} + 3.4×10^{-6} V^2_{shock}). The data points over-plotted with triangles indicate shocks associated with slow CMEs (initial speed, $V_{CME} \leq 375$ kms^{-1}). The filled circles represent CMEs that interact with preceding CMEs.

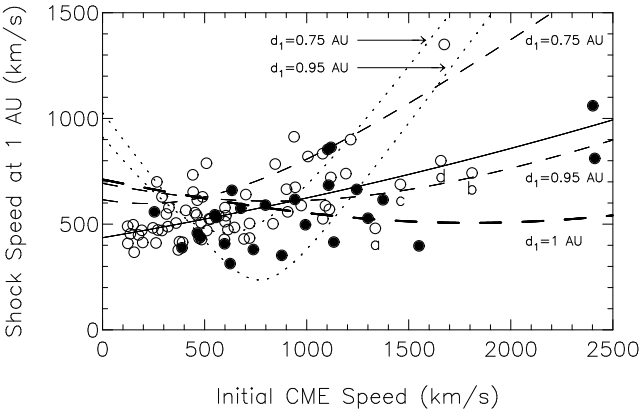

Figure 3. Observed IP shock speed at 1 AU plotted against initial speed of the CME. The interacting CMEs are shown by filled circles. The dotted lines are based on the linear-acceleration model (equation 1) and dashed curves are from the quadratic form of acceleration (equation 2) given by *Gopalswamy et al.* [2001] for different acceleration-cessation distances, d_1, (in the upper to lower order, dotted curves are for $d_1 = 0.75$ and 0.95 AU and dashed curves are for $d_1 = 0.75$, 0.95, and 1 AU). The best-fit is shown by solid line (equation 3). The points marked with letters a, b, c, and d are also interacting cases (see Section 3). On the whole, these data points show a correlation of ~60% between the CME speed and shock speed.

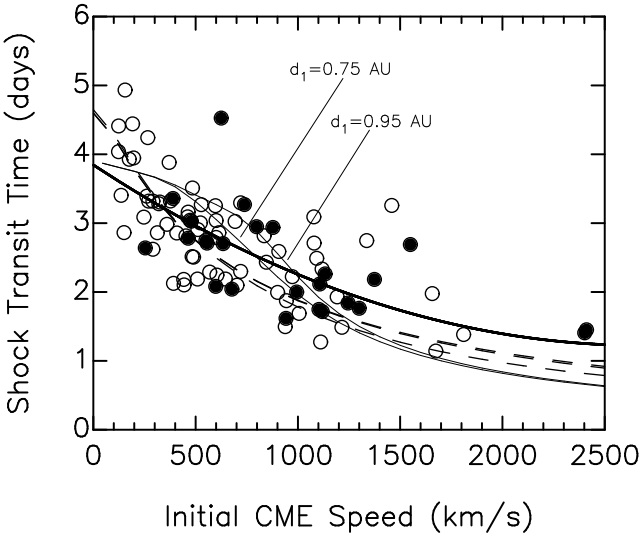

Figure 4. IP shock transit time to 1 AU as a function of initial speed of the CME. The interacting CMEs are shown by filled circles. The thick-solid line is the best least square fit to the data points. The thin solid-line curves and dashed curves are based on arrival time predictions given by *Gopalswamy et al.* [2001], respectively, assuming constant acceleration (shown by thin curves for $d_1 = 0.75$ and 0.95 AU) and second-order fit (shown by dashed curves for $d_1 = 0.75$, 0.95, and 1 AU). The difference between the dashed curves corresponding to $d_1 = 0.95$ and 1 AU is small and they overlap with each other in the entire range of speed. The difference in the dashed-line curves can only be seen in the high-speed tail part and the curve corresponding to $d_1 = 0.75$ lies in the smaller transit time region. However, curves of greater distances (0.95 and 1 AU), for a given high speed, show a longer travel time than the above.

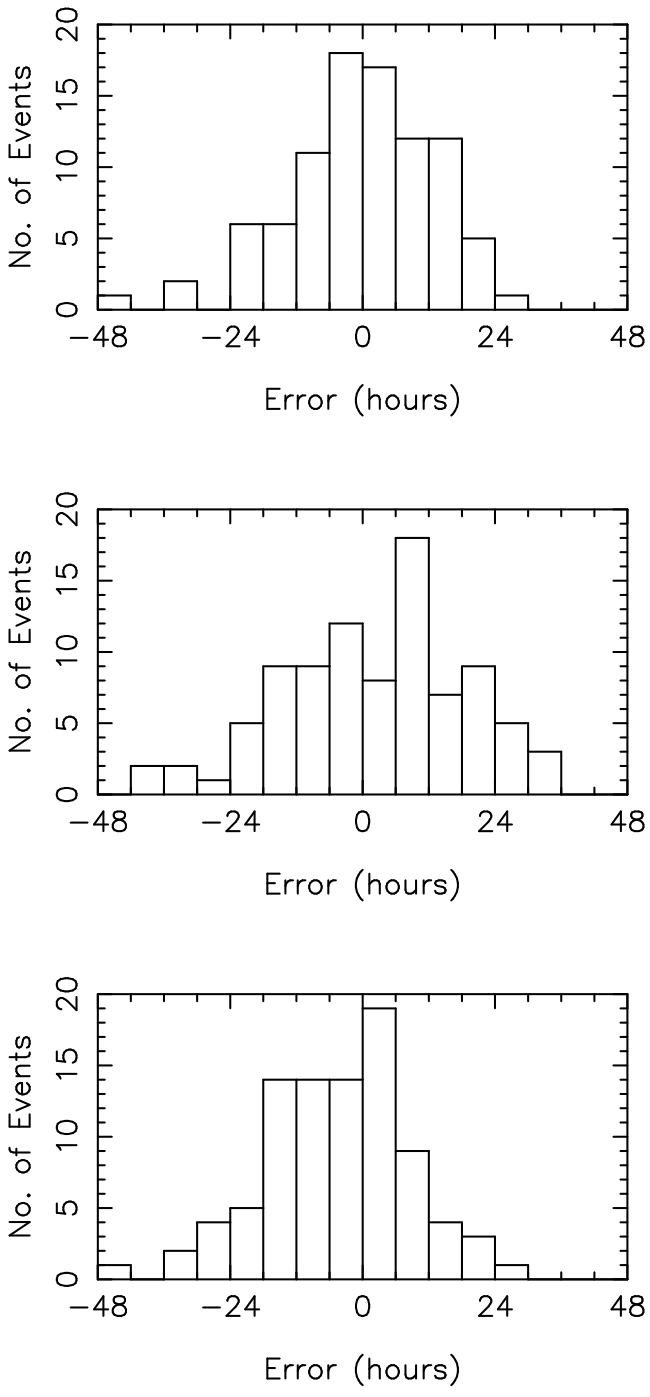

Figure 5. Histograms showing the distribution of arrival time deviation (difference between model and observed travel times) for empirical model given in equation 4 (top), equation 1 (middle), and equation 2 (bottom). Mean absolute value of deviations for these distributions are 10, 14, 11 hours, from top to bottom.

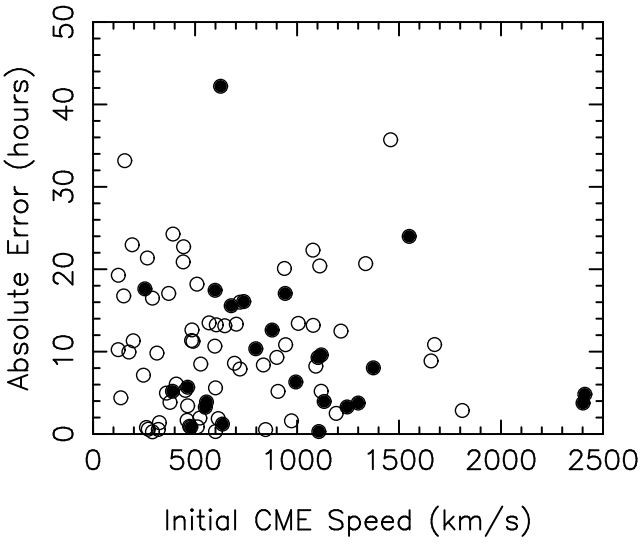

Figure 6. Absolute arrival time difference (between the empirical model given in equation 4 and observed values) shown as a function of white-light CME speed. Large deviations are due to CMEs having speeds, V_{CME}<450 and >850 kms^{-1}.

Table 1. List of IP Shocks and Associated CMEs

	IP Shock						ICME			White-light CME				
No.	Date	Time h:m	V_{SH} km/s	M_a	M_s	TT hr	Date	Time h:m	V_{EJ} km/s	Date	Time h:m	H/P	V_{CME} km/s	Loc
1	970110	0052	454	3.8	2.6	81.7	970110	0500	436	970106	1510	H	136	S18E06
2	970209	1240	629	3.0	1.7	60.2	970210	0300	460	970207	0030	H	490	S20W04
3	970410	1255	352	1.1	1.0	70.5	970411	0600	470	970407	1427	H	878	S28E19[I]
4	970515	0115	458	4.0	3.3	66.7	970515	0900	450	970512	0630	H	464	N21W08[I]
5	970902	2240	378	2.2	1.4	93.2	970903	1200	400	970830	0130	H	371	N30E17
6	970921	0410	417	1.9	1.8	79.7	970921	2200	425	970917	2028	H	377	N30W10
7	971122	0910	497	4.1	2.7	68.7	971122	1400	490	971119	1227	P	150	N20E05
8	971230	0115	413	2.0	1.8	94.7	971230	1800	370	971226	0231	P	197	N24E14
9	980128	1600	430	1.9	1.4	72.6	980129	1345	390	980125	1526	H	693	N21E25
10	980218	0750	490	1.4	1.4	96.9	980218	2110	370	980214	0655	P	123	S24E23
11	980304	1105	449	3.2	2.4	94.3	980304	1400	360	980228	1248	P	176	S24W01
12	980407	1655	367	1.6	1.5	118.4	980407	1715	325	980402	1830	P	155	S23E23
13	980501	2120	615	2.5	2.1	52.4	980502	1200	515	980429	1658	H	1374	S18E20[I]
14	980504	0200	913	6.6	4.2	35.9	980504	1200	650	980502	1406	H	938	S15W15
15	980613	1920	409	1.9	1.8	105.9	980614	0300	350	980609	0927	P	124	S25W20
16	980625	1610	471	1.1	1.1	106.6	980626	0200	475	980621	0535	P	192	N17W25
17	981018	1928	411	2.6	2.0	81.4	981019	0500	383	981015	1004	H	262	N22W01
18	981107	0800	525	2.1	1.7	72.1	981107	2300	475	981104	0754	H	523	N17W01
19	981108	0442	721	1.4	1.4	56.0	981108	0900	620	981105	2044	H	1118	N22W18
20	981113	0140	578	3.3	2.9	79.4	981113	1200	400	981109	1818	P	325	N15W05
21	990310	0130	502	2.4	1.8	67.6	990310	1900	435	990307	0554	P	835	S20E15
22	990416	1110	470	1.5	1.4	79.7	990416	2000	406	990413	0330	H	291	N16E00
23	990702	0023	660	2.7	2.3	64.9	990702	2200	600	990629	0731	H	634	N19E02[I]
24	990804	0146	415	1.8	1.7	54.3	990804	2030	340	990801	1927	P	1133	N25E13[I]
25	990915	0743	700	2.7	2.0	101.8	990915	1700	575	990911	0154	P	266	S20W30
26	990915	2000	652	2.1	1.6	50.5	990916	0300	575	990913	1731	P	444	N15E06
27	990922	1200	540	2.7	2.3	53.9	990922	1930	500	990920	0606	H	604	S20W05
28	991021	0213	482	2.8	2.6	74.1	991021	0500	500	991018	0006	P	247	S30E15
29	991028	1210	470	1.6	1.3	69.7	991029	0300	380	991025	1426	P	511	S20E05
30	000122	0023	380	1.4	1.1	78.5	000122	1750	400	000118	1754	H	739	S19E11[I]
31	000211	0233	525	1.8	1.8	65.0	000211	1700	425	000208	0930	H	1079	N25E26
32	000211	2328	674	3.9	3.4	45.0	000212	1654	543	000210	0230	H	944	N30E04
33	000214	0718	684	1.7	1.3	50.8	000214	1230	550	000212	0431	H	1107	N26W23[I]
34	000220	2100	512	3.2	3.0	72.9	000221	0948	380	000217	2006	H	600	S25W12
35	000604	1453	733	4.8	4.2	52.4	000605	0000	470	000602	1030	H	442	N10E23
36	000608	0904	863	5.3	3.9	41.2	000608	1700	760	000606	1554	H	1119	N20E15[I]
37	000623	1300	613	2.7	2.3	75.8	000624	0800	580	000620	0910	P	464	S30W30
38	000710	0600	554	1.7	1.6	67.6	000711	0130	440	000707	1026	H	453	N17E10
39	000711	1210	507	1.5	1.4	60.3	000712	0000	540	000708	2350	P	483	N18W12
40	000714	1539	833	2.4	2.1	74.2	000715	0600	650	000711	1327	H	1078	N17E27

Table 1. Continued

	IP Shock						ICME			White-light CME				
No.	Date	Time h:m	V_{SH} km/s	M_a	M_s	TT hr	Date	Time h:m	V_{EJ} km/s	Date	Time h:m	H/P	V_{CME} km/s	Loc
41	000715	1418	1350	7.5	6.9	27.4	000715	1900	990	000714	1054	H	1674	N22W07
42	000728	0639	488	2.2	2.2	78.7	000728	1500	460	000724	2354	P	320	N05W10
43	000728	0958	523	1.4	1.4	78.5	000728	2100	471	000725	0330	H	528	N06W08
44	000810	0510	428	1.1	1.0	78.1	000810	2100	400	000806	2306	P	597	S20W30
45	000811	1851	640	1.7	1.6	50.4	000812	0600	567	000809	1630	H	702	N11W11
46	000915	0428	397	2.5	2.0	64.6	000915	1630	375	000912	1154	H	1550	S12W18[I]
47	000917	1700	900	2.2	1.8	35.7	000918	0100	760	000916	0518	H	1215	N14W07
48	001005	0323	538	3.2	3.0	55.0	001005	1600	510	001002	2026	H	569	S09E07
49	001012	2236	590	4.7	4.3	70.8	001013	1700	395	001009	2350	H	798	N01W14[I]
50	001106	0920	629	2.1	1.8	62.9	001106	2300	535	001103	1826	H	291	N02W02
51	001126	0530	497	2.4	2.0	48.0	001126	0800	475	001124	0530	H	994	N20W05[I]
52	001126	1140	664	2.5	1.9	44.2	001127	1230	575	001124	1530	H	1245	N22W07[I]
53	010220	0230	313	2.6	1.5	108.6	010220	2000	350	010215	1354	H	625	N07E12[I]
54	010303	1130	548	2.2	1.8	68.7	010304	0300	475	010228	1450	P	313	S02W12
55	010319	1130	472	2.8	2.4	79.7	010319	2200	360	010316	0350	P	271	N11W09
56	010322	1400	388	1.5	1.4	80.6	010322	2230	390	010319	0526	H	389	S05W00[I]
57	010327	1805	575	1.5	1.3	49.0	010328	0730	600	010325	1706	H	677	N16E25[I]
58	010331	0114	617	9.0	5.8	38.8	010331	0500	650	010329	1026	H	942	N14W12[I]
59	010411	1412	739	2.9	2.3	46.3	010411	2118	670	010409	1554	H	1192	S21W04
60	010411	1619	811	1.7	0.9	34.8	010412	0500	700	010410	0530	H	2411	S23W09[I]
61	010413	0725	853	1.7	1.6	41.9	010413	1330	800	010411	1331	H	1103	S22W27[I]
62	010421	1530	414	2.1	1.7	51.0	010422	0048	395	010419	1230	P	392	N20W20
63	010428	0502	820	4.0	3.7	40.5	010429	0148	640	010426	1230	H	1006	N17W00
64	010812	1110	438	3.4	2.7	72.7	010813	0800	400	010809	1030	P	479	N05W05[I]
65	010830	1400	565	1.7	1.6	68.6	010830	2000	440	010827	1726	P	408	N10W30
66	010914	0200	484	2.8	2.6	52.5	010914	1600	400	010911	2130	P	646	S00E05
67	010925	2018	1060	8.7	8.4	33.8	010926	1000	600	010924	1030	H	2402	S12E23[I]
68	010929	0925	788	4.5	3.0	52.5	010929	1500	700	010927	0454	P	509	S20W27
69	010930	1915	784	6.7	5.9	58.3	010931	0000	530	010928	0854	H	846	N10E18
70	011011	1650	588	3.1	3.0	53.3	011012	0330	550	011009	1130	H	973	S28E08
71	011021	1640	665	6.4	4.2	47.8	011022	0100	660	011019	1650	H	901	N15W29
72	011025	0900	480	4.4	3.9	65.9	011025	1800	430	011022	1506	H	1336	S21E18
73	011028	0310	587	2.4	2.4	59.7	011028	1100	460	011025	1526	H	1092	S16W21
74	011031	1347	407	1.7	1.6	49.9	011031	2118	340	011029	1150	P	598	N12E25[I]
75	011106	0145	742	-	3.2	33.2	011106	1900	700	011104	1635	H	1810	N06W18
76	020217	0330	433	3.2	2.5	73.0	020217	0800	425	020214	0230	P	473	N18E04
77	020318	1313	558	8.0	5.3	62.1	020319	0600	370	020315	2306	H	907	S08W03
78	020323	1124	544	2.6	2.3	65.9	020324	0348	440	020320	1730	P	550	S17W20[I]
79	020417	1101	503	4.2	3.3	55.2	020417	2100	600	020415	0350	H	720	S15W01
80	020510	1110	434	1.4	1.2	79.1	020510	2200	350	020507	0406	H	720	S10E27

Table 1. Continued

	IP Shock						ICME			White-light CME				
No.	Date	Time h:m	V_{SH} km/s	M_a	M_s	TT hr	Date	Time h:m	V_{EJ} km/s	Date	Time h:m	H/P	V_{CME} km/s	Loc
81	020511	1030	474	3.1	2.6	68.7	020512	0100	500	020508	1350	H	614	S12W07
82	020518	1951	578	6.5	5.1	67.0	020519	0348	458	020516	0050	H	600	S22E14
83	020520	0340	543	1.5	1.4	74.2	020520	1500	450	020517	0127	P	461	S20E05
84	020717	1550	528	2.6	2.1	42.3	020718	1200	450	020715	2130	H	1300	N19W01[I]
85	020719	1440	570	1.1	1.0	30.6	020720	0900	700	020718	0806	H	1111	N19w30
86	020801	0510	532	1.3	1.3	65.0	020801	1148	454	020729	1207	H	556	N10W15[I]
87	020801	2305	505	1.4	1.3	71.6	020802	0718	493	020729	2330	P	360	S10W10
88	020818	1840	688	8.5	4.8	54.2	020819	0600	525	020816	1230	H	1459	S14E20
89	020820	1350	558	1.3	1.3	63.3	020821	0000	425	020817	2230	P	254	S06W05[I]
90	020907	1620	800	4.9	4.8	47.4	020908	0400	500	020905	1654	H	1657	N04W28
91	021109	1820	427	1.8	1.7	84.2	021110	0900	375	021106	0606	P	485	S13E13

columns 2 – 6: shock arrival date, time (hr:mt), speed (kms^{-1}), Alfvenic (M_a), magnetosonic (M_s) Mach numbers.
column 7: shock transit time in hours.
columns 8 – 10: ICME arrival date, time (hr:mt), and speed (kms^{-1}).
columns 11 – 15: white-light CME date, time (hr:mt), type (Halo/Partial halo), speed (kms^{-1}), and location.
[I] CME interacts with preceding CME(s)

Table 2. Ranges and Average Values

	All events		Interacting cases	
Parameter	min – max	avg	min – max	avg
V_{SHOCK} (kms^{-1})	313 – 1350	574	313 – 1060	568
t_{SHOCK} (days)	1.14 – 4.93	2.70	1.41 – 4.53	2.42
V_{ICME}, (kms^{-1})	325 – 990	496	340 – 800	500
t_{ICME} (days)	1.34 – 5.25	3.17	1.77 – 5.25	2.96
V_{CME} (kms^{-1})	123 – 2411	732	254 – 2411	973